C-start: optimal start of larval fish

M. Gazzola, W. M. Van Rees and P. Koumoutsakos†

Institute of Computational Science, ETH Zürich, Universitätsstrasse 6, CH-8092 Zürich, Switzerland

We investigate the C-start escape response of larval fish by combining flow simulations using remeshed vortex methods with an evolutionary optimization. We test the hypothesis of the optimality of C-start of larval fish by simulations of larval-shaped, two- and three-dimensional self-propelled swimmers. We optimize for the distance travelled by the swimmer during its initial bout, bounding the shape deformation based on the larval mid-line curvature values observed experimentally. The best motions identified within these bounds are in good agreement with *in vivo* experiments and show that C-starts do indeed maximize escape distances. Furthermore we found that motions with curvatures beyond the ones experimentally observed for larval fish may result in even larger escape distances. We analyse the flow field and find that the effectiveness of the C-start escape relies on the ability of pronounced C-bent body configurations to trap and accelerate large volumes of fluid, which in turn correlates with large accelerations of the swimmer.

Key words: propulsion, swimming/flying

1. Introduction

Fish burst accelerations from rest are often observed in predator–prey encounters. These motions may be distinguished into C- and S-starts, according to the bending shape of the swimmer. Predators mainly exhibit S-starts during an attack, while C-starts are typical escaping mechanisms observed in prey (Domenici & Blake 1997). Since the first detailed report by Weihs (1973), C-start behaviour has attracted much attention with studies considering the resulting hydrodynamics and the kinematics of these motions (Domenici & Blake 1997; Budick & O'Malley 2000; Muller & van Leeuwen 2004; Muller, van den Boogaart & van Leeuwen 2008) in experiments (Tytell & Lauder 2002; Epps & Techet 2007; Muller *et al.* 2008; Conte *et al.* 2010) and simulations (Hu *et al.* 2004; Katumata, Muller & Liu 2009).

Several works have suggested that C-start is an optimal escape pattern (Howard 1974; Weihs & Webb 1984; Walker *et al.* 2005), but to the best of our knowledge, this has been an observation and not the result of an optimization study. The goal of the present work is to perform an optimization of the fish motion, for a specified zebrafish-like geometry, maximizing the distance travelled over few tail beats by a swimmer starting from rest. The optimization couples the covariance matrix adaptation evolution strategy (Hansen, Muller & Koumoutsakos 2003) with two-dimensional and

† Email address for correspondence: petros@inf.ethz.ch

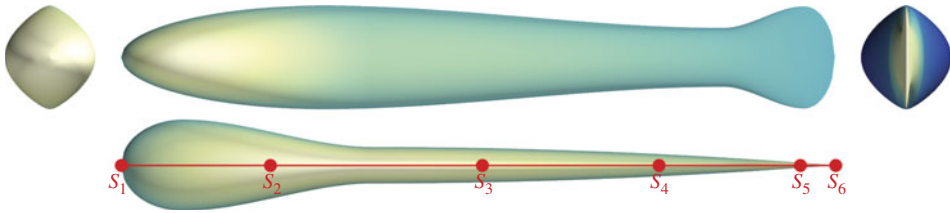FIGURE 1. (Colour online available at journals.cambridge.org/flm) Side, top, front and rear view of the implemented geometrical model of the zebrafish larva. On the top view, from left to right, the six curvature control points $S_1 = 0$, $S_2 = 0.2L$, $S_3 = 0.5L$, $S_4 = 0.75L$, $S_5 = 0.95L$, $S_6 = L$ are indicated.

three-dimensional flow simulations using a remeshed vortex method with penalization (Coquerelle & Cottet 2008; Gazzola *et al.* 2011*a*).

The paper is organized as follows: the geometrical model and motion parameterization of the swimmer is presented in §2 and the optimization procedure and the numerical method in §3. We discuss the flow characteristics for the best parameter sets in two and three dimensions in §4, and summarize our findings in §5.

2. Geometrical model and motion parameterization

Inspired by the experimental study of zebrafish larva motion (Muller *et al.* 2008), we consider a two-dimensional swimmer with a similar shape described by the half-width $w(s)$ of the body along its arc-length s. In the three-dimensional case, the geometry is described in terms of elliptical cross-sections of height $h(s)$ and width $w(s)$. The piecewise continuous functions characterizing the half-width $w(s)$ and height $h(s)$ (appendix A – larva's geometry) aim to reproduce the geometry of a 4.4 mm long larva zebrafish of age 5 days post-fertilization (Fontaine *et al.* 2008; Muller *et al.* 2008; Parichy *et al.* 2009) (figure 1). The motion pattern of a fish performing a C-start is characterized by two phases (Domenici & Blake 1997; Muller *et al.* 2008). The first phase, denoted the preparatory stroke, consists of the formation of the C-shape. When the fish is fully bent, the second phase involves a propulsive stroke and a backflip of the tail to propel the fish forward. The fast start can then be followed by either continuous swimming or coasting (Domenici & Blake 1997; Muller *et al.* 2008).

In this study, we employ a parameterization that entails these two phases, leading to a continuous swimming pattern, while the motion parameters are determined by the optimizer. The parameterization is based on the instantaneous curvature κ_s along the mid-line s of the swimmer (Kern & Koumoutsakos 2006), adapted to account for the two phases:

$$\kappa_s(s, t) = B(s) + K(s) \sin[2\pi(t/T_{prop} - \tau(s)) + \phi], \qquad (2.1)$$

where $B(s)$ and $K(s)$ are natural cubic splines through the curvature values B_i and K_i at the m interpolation points S_i $(i = 1, \ldots, m)$ along the body of the fish, ϕ is the phase, t is the time, and T_{prop} is the swimming or propulsive period. The phase shift $\tau(s)$ is linearly proportional to the arc-length $\tau(s) = (s/L)\tau_{tail}$ and is responsible for a travelling wave along the body of the fish.

Hence, the fish starting motion is parameterized by two sets of curvatures, hereafter denoted baseline curvature $\boldsymbol{B} = \{B_1, \ldots, B_m\}$ and undulatory curvature $\boldsymbol{K} = \{K_1, \ldots, K_m\}$. The fish starts from an undisturbed position and within the preparatory time interval T_{prep}, transitions to the configuration determined by $\boldsymbol{B}$ and $\boldsymbol{K}$.

After this stage the preparatory stroke is completed and the fish transitions (within T_{prop}) to the propulsive configuration, completing its first swimming motion cycle. By the end of this cycle, at $t = T_{prep} + T_{prop}$, the baseline curvature has returned to zero, and another cycle follows which is solely determined by the curvature $\boldsymbol{K}$. Each transition from one configuration to another is carried out through a cubic interpolation between start and end curvature (setting the first derivative at the extrema to zero to ensure smoothness) within the prescribed time interval. The parameter τ_{tail} is also ramped up via cubic interpolation from zero to its designated value at T_{prep}. We note that the use of a baseline curvature $\boldsymbol{B}$ arises from the observation that the C-start motion is not periodic, as it would be if only undulatory curvature $\boldsymbol{K}$ were to be considered. Therefore $\boldsymbol{B}$ enables the model to capture a broader range of deformations, thus enlarging the reproducible set of possible motions.

We use six control points located at $S_1 = 0$, $S_2 = 0.2L$, $S_3 = 0.5L$, $S_4 = 0.75L$, $S_5 = 0.95L$, $S_6 = L$ (figure 1) and the curvature at S_1, S_2 and S_6 is set to zero. These locations and curvature constraints are chosen to model the stiff head, the increasing flexibility towards the posterior of the body and the stiff last fraction of the tail (Muller & van Leeuwen 2004; Fontaine *et al.* 2008; Muller *et al.* 2008). Furthermore, we fix the ratio between the preparatory and propulsive time interval to $T_{prep}/T_{prop} = 0.7$, based on the experimental observations of Muller *et al.* (2008) and Budick & O'Malley (2000), and set $T_{prep} + T_{prop} = 1$ physical time unit. During the optimization we reject cases where $|\kappa_s(s, t)| > 2\pi/L$. These curvature constraints conform with the range of curvature values experimentally observed in fast starts of larval zebrafish (Muller *et al.* 2008), even though they may not be directly related to larval biomechanical properties.

In summary, the fish starting motion is characterized by eight free parameters, namely B_3, B_4, B_5, K_3, K_4, K_5, τ_{tail}, and ϕ, which will be varied during the optimization. We emphasize that biomechanics is not considered in our model and flow-induced body deformations are not accounted for in this study.

3. Optimization of starting motion

Based on extensive experimental observations, Domenici & Blake (1997) emphasized that the quantities relevant to evaluating fast starts are distance or speed attained and the time interval of such responses. Therefore we chose to identify the starting motion pattern (characterized by $\boldsymbol{B}$, $\boldsymbol{K}$, τ_{tail}, and ϕ) via the optimization of the maximum distance travelled by the centre of mass of the swimmer (d_{max}^T) in the time interval $[0, T = T_{prep} + 2T_{prop}]$. Within this interval, the fish performs the preparatory stroke, the propulsive stroke and one additional swimming cycle. This time interval is chosen so as to capture the full start while also allowing examination of the final swimming pattern. The identification of the optimal parameter set is cast into a minimization problem where the cost function is defined as $f = -|d_{max}^T|$.

The optimization is performed using the covariance matrix adaptation evolutionary strategy (CMA-ES) in its multi-host, rank-μ and weighted recombination form (Hansen *et al.* 2003; Gazzola, Vasilyev & Koumoutsakos 2011*b*). Evolution strategies have been shown to be effective in dealing with computational and experimental, single and multi-objective, flow optimization problems (Buche *et al.* 2002; Kern & Koumoutsakos 2006; Gazzola *et al.* 2011*b*). The CMA-ES is an iterative algorithm that operates by sampling, at each generation, p candidate parameter vectors from a multivariate Gaussian distribution $\mathcal{N}(\boldsymbol{m}, \sigma^2\boldsymbol{C})$. Its mean $\boldsymbol{m}$, overall standard deviation σ and covariance matrix $\boldsymbol{C}$ are adapted based on past successful parameter vectors,

ranked according to their cost function values. We note that de-randomized evolution strategies do not ensure that the global optimum is found. In turn the robustness of CMA-ES is mainly controlled by the population size p (Hansen *et al.* 2003). Here, as a tradeoff between robustness and fast convergence, we set $p = 100$ for the two-dimensional case, while for the three-dimensional case, given the higher computational costs, we reduced it to $p = 40$. The search space is bounded for all curvature parameters by $[-2\pi/L, 2\pi/L]$, and for τ_{tail} and ϕ by $[0, 2\pi]$ (furthermore $|\kappa_s(s, t)| \leqslant 2\pi/L$ at all times and invalid configurations are discarded). Bounds are enforced during the sampling through a rejection algorithm. The initial parameter vector was set to $\mathbf{0}$ for the two-dimensional case, while for the three-dimensional case, we started from the best parameter set found during the two-dimensional optimization. Initial standard deviations were set to $1/15$ of the corresponding search space interval.

3.1. *Equations and numerical method*

We consider a deforming and self-propelling body in a viscous incompressible flow determined by solving the incompressible Navier–Stokes equations:

$$\frac{\partial \mathbf{u}}{\partial t} + (\mathbf{u} \cdot \nabla) \mathbf{u} = -\frac{1}{\rho} \nabla p + \nu \nabla^2 \mathbf{u}, \quad \mathbf{x} \in \Sigma \setminus \Omega, \tag{3.1}$$

where ρ is the fluid density (set equal to body density), ν the kinematic viscosity, Σ the computational domain and Ω the support of the body. The action of the body on the fluid is realized through the no-slip boundary condition at the interface $\partial\Omega$, enforcing the body velocity ($\mathbf{u}_s$) to be the same as the fluid velocity ($\mathbf{u}$). The feedback from the fluid to the body is in turn described by Newton's equation of motion $m_s \ddot{\mathbf{x}}_s = \mathbf{F}$ and $\mathrm{d}(\mathbf{I}_s \boldsymbol{\theta}_s)/\mathrm{d}t = \mathbf{M}$, where $\mathbf{x}_s$, $\boldsymbol{\theta}_s$, m_s, $\mathbf{I}_s$, $\mathbf{F}$ and $\mathbf{M}$ are, respectively, the body's centre of mass, angular velocity, mass, moment of inertia and hydrodynamic force and momentum exerted by the fluid on the body.

The flow is solved via a remeshed vortex method, characterized by a Lagrangian particle advection, followed by particle remeshing and the use of an FFT-based Poisson solver (Koumoutsakos & Leonard 1995; Koumoutsakos 1997). The remeshed vortex method was coupled to Brinkman penalization, a projection approach handles the feedback from the flow to the body, while the body surface is tracked implicitly by a level set (Coquerelle & Cottet 2008). The penalization term added to the Navier–Stokes equations approximates the no-slip boundary condition at the body interface, and allows the control on the solution error through the penalization factor λ. This algorithm has been extended to non-divergence-free deformations for single and multiple bodies (Gazzola *et al.* 2011*a*).

Equation (3.1) is cast into its velocity ($\mathbf{u}$)–vorticity ($\boldsymbol{\omega} = \nabla \times \mathbf{u}$) formulation

$$\frac{\partial \boldsymbol{\omega}}{\partial t} + \nabla \cdot (\mathbf{u} : \boldsymbol{\omega}) = (\boldsymbol{\omega} \cdot \nabla)\mathbf{u} + \nu \nabla^2 \boldsymbol{\omega} + \lambda \nabla \times \chi_s(\mathbf{u}_s - \mathbf{u}), \quad \mathbf{x} \in \Sigma, \tag{3.2}$$

where $\nabla \cdot (\mathbf{u} : \boldsymbol{\omega})$ is the vector with components $\partial/\partial x_i(u_i\omega_j)$, χ_s the characteristic function (Gazzola *et al.* 2011*a*) describing the body shape and $\lambda \gg 1$ the penalization factor (here $\lambda = 10^4$ and the mollification length of χ_s is $\epsilon = 2\sqrt{2}h$, h being the grid spacing). Translational ($\mathbf{u}_T$) and rotational ($\mathbf{u}_R$) components of $\mathbf{u}_s = \mathbf{u}_T + \mathbf{u}_R + \mathbf{u}_{DEF}$ are recovered through a projection approach. The deformation velocity $\mathbf{u}_{DEF}$ (prescribed *a priori*) is specific to the shape under study. As $\mathbf{u}_{DEF}$ is in general non-solenoidal, the
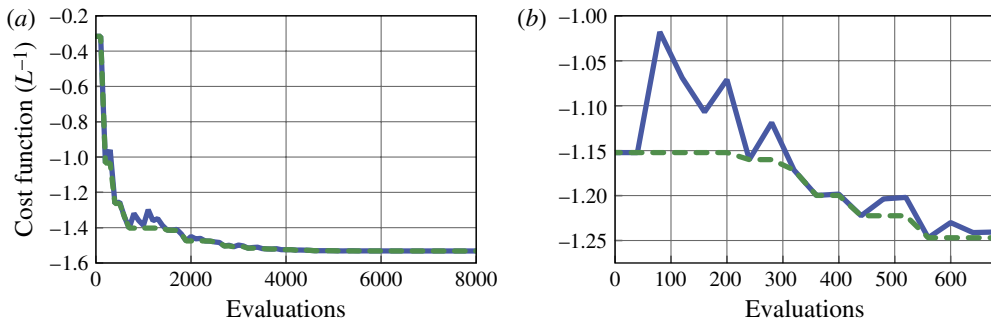
FIGURE 2. (Colour online) Cost function value f (normalized by L) against number of evaluations: two-dimensional (*a*) and three-dimensional (*b*) optimizations. Solid (blue online) and dashed (green online) lines correspond to, respectively, best solution in the current generation and best solution ever. The best two-dimensional solution was used as starting search point in the three-dimensional case.

	B_3	B_4	B_5	K_3	K_4	K_5	τ_{tail}	ϕ	f
Best two-dimensional	-3.19	-0.74	-0.44	-5.73	-2.73	-1.09	0.74	1.11	-1.53
Best three-dimensional	-1.96	-0.46	-0.56	-6.17	-3.71	-1.09	0.65	0.83	-1.25

TABLE 1. Best motions identified through the optimization (curvatures normalized by L).

incompressibility constraint becomes $\nabla \cdot \boldsymbol{u} = 0$ for $\boldsymbol{x} \in \Sigma \setminus \Omega$ and $\nabla \cdot \boldsymbol{u} = \nabla \cdot \boldsymbol{u}_{DEF}$ for $\boldsymbol{x} \in \Omega$. This translates into recovering $\boldsymbol{u}$ from the Poisson equation $\nabla^2 \boldsymbol{u} = -\nabla \times \boldsymbol{\omega} + \nabla(\nabla \cdot \boldsymbol{u}_{DEF})$, with unbounded boundary conditions (Gazzola *et al.* 2011*a*).

During the course of the optimization in two dimensions, simulations were carried out in a domain $[0, 4L] \times [0, 4L]$, with constant resolution 1024×1024 and Lagrangian CFL set to 0.1. Quantities of interest were recomputed at higher resolution (2048×2048). In the three-dimensional case, simulations were carried out in a domain of variable size, growing in time to accommodate the wake. The grid spacing was kept constant at $\delta x = L/256$ during the optimization and at $\delta x = L/512$ for the higher-resolution runs that resulted in the reported diagnostics.

3.2. *Flow conditions*

We define the Reynolds number as $Re = (L^2/T_{prop})/\nu$, where L is the fish length and T_{prop} is the swimming period. Here we consider a body that models a zebrafish larva of length $L = 4.4$ mm, corresponding to a fish of age 5 days post-fertilization (Muller *et al.* 2008; Parichy *et al.* 2009). For a typical swimming period of $T_{prop} \approx 44$ ms (Muller *et al.* 2008) in water, we obtain a Reynolds number $Re = 550$ and our simulations were performed at this Reynolds number.

4. Results

4.1. *Two-dimensional swimmer*

The course of the optimization for the two-dimensional swimmer is shown in figure 2(*a*) and the best parameter set is presented in table 1. This parameter set induces the motion sequence illustrated in figures 3 and 4. The solution found closely
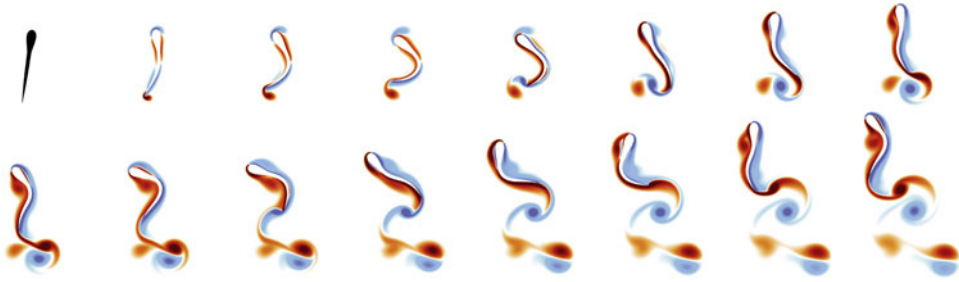
FIGURE 3. (Colour online) Vorticity fields of the two-dimensional best solution (blue negative and red positive vorticity) time sequence ($0 \leqslant t \leqslant 2.35 T_{prop}$; $\Delta t = 0.156 T_{prop}$).
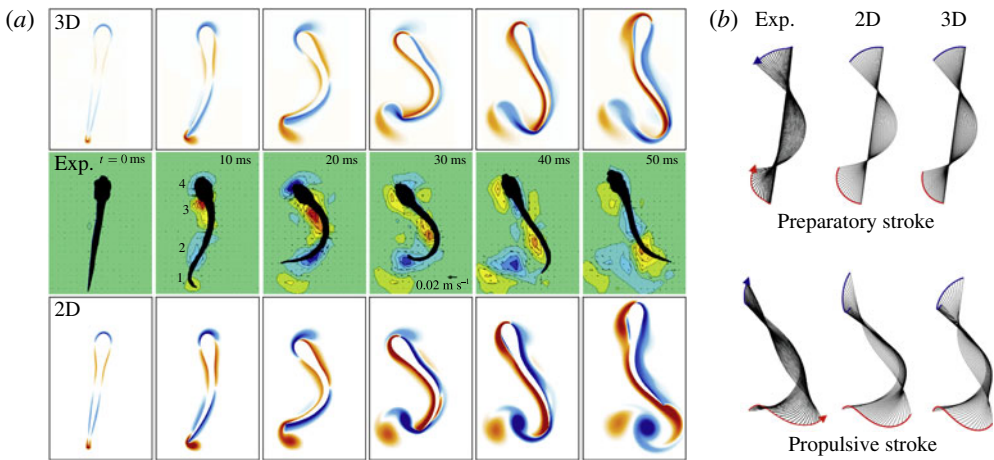

FIGURE 4. (Colour online) Zebrafish larva C-start, experiments and simulations. (*a*) Vorticity fields (blue negative and red positive vorticity) and (*b*) swimming kinematics, represented by body mid-lines, corresponding to the best two-dimensional (2D) and three-dimensional (3D) solutions found via the optimization procedure and experimental observations by Muller *et al.* (2008).

reproduces the starting bout observed experimentally in larval zebrafish (Muller *et al.* 2008). During the preparatory stroke, the fish bends into a C-shape, then straightens to propel itself forward and completes its cycle.

In order to further quantify C-start mechanics and to elucidate its hydrodynamics, we considered, at time $t_A = T_{prep} + T_{prop}$ and $t_B = T_{prep} + 2T_{prop}$, respectively, the first (A) and second (B) vortex pair generated by nine different motion patterns (figure 5). The reference motion pattern is defined by the best parameters as found by the optimization process (case 0). We systematically increased/decreased the curvature K^{2D}_{best} and B^{2D}_{best} corresponding to the best solutions found (cases -3 to 4 as detailed in figure 5) in order to assess the impact of the C-curvature on the flow. We note that cases -3, -2, -1 lie outside the parameter search space of the optimization (since $K_3 > 2\pi/L$). These cases are included in order to explore the effect of curvature values beyond those reported experimentally. Furthermore, in case 5 we considered as reference a 'slow start' performed by anguilliform swimming, an archetypal mode of locomotion characterized by the propagation of curvature waves from the anterior to
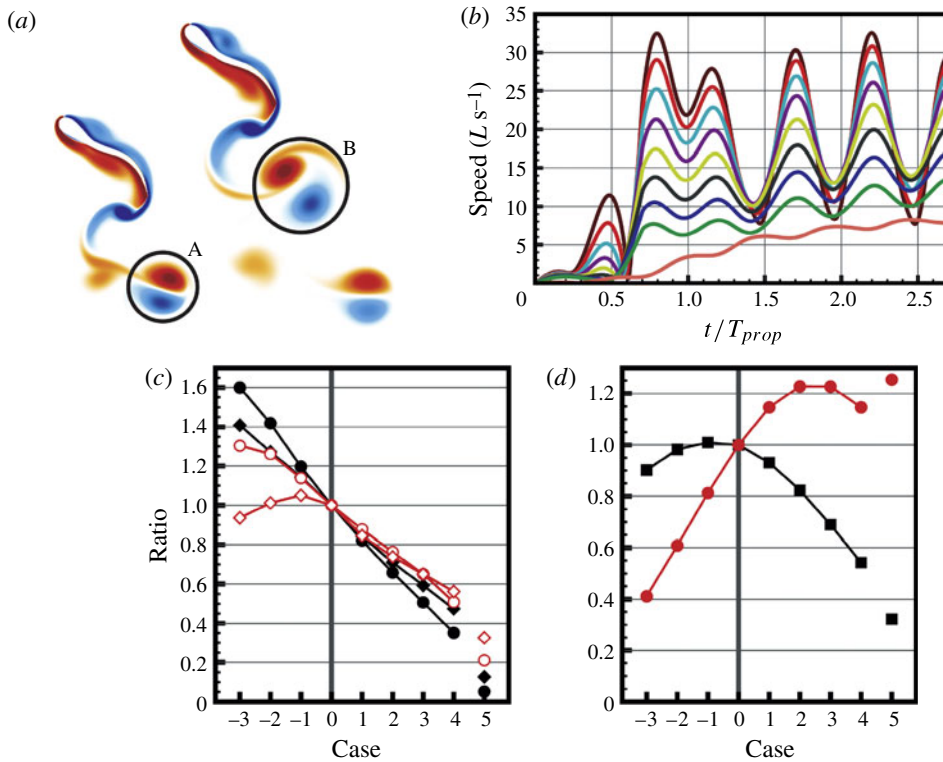
FIGURE 5. (Colour online) Vortex pair characterization in the two-dimensional setup. Nine motions are considered: the maximum found (case 0), motions with enhanced/reduced curvature with respect to case 0 (130 %, 120 %, 110 %, 90 %, 80 %, 70 %, 60 %, respectively, case -3, -2, -1, 1, 2, 3, 4), and (case 5) cruise swimming. (*a*) First (A) and second (B) vortex pairs at time, respectively, $t_A = T_{prep} + T_{prop}$ and $t_B = T_{prep} + 2T_{prop}$, for case 0. (*b*) Speed of the fish centre of mass, from top to bottom, cases -3 to 5, expressed in length/seconds, based on a zebrafish of $L = 4.4$ mm and $T_{prop} \approx 44$ ms in water. (*c*) Vortex pairs' (A, circle; B, diamond) relative total circulation ($|\Gamma|/|\Gamma_0|$, black) and area ($|A|/|A_0|$, red) with respect to case 0, versus all cases. Vortex cores in A/B, are localized via the criterion $|\omega| > 0.15 \max |\omega_0|$, where $\max |\omega_0|$ is the maximum vorticity of structure A/B in case 0. (*d*) Relative distance travelled (f/f_0, black) and energetic efficiency (η/η_0, red).

the posterior of the body. We used the kinematic description given in Gazzola *et al.* (2011*a*) along with a cubic interpolation to ramp up the motion within T_{prep}. As can be seen in figure 5, areas and circulations $|\Gamma|$ of the shed vortex pairs A and B monotonically decrease with reducing curvature magnitude, except for the area of the vortical structure B which shows a maximum for case -1. In case 5 the areas and circulations, of structures A and B, are found to be substantially smaller than in all other cases. Figure 5(*b*) shows that the fish achieves larger speed on increasing the curvature, indicating a correlation between the strength of vortex cores and speed. However, speed does not necessarily translate into a larger distance travelled by the centre of mass, due to increased lateral velocities, as depicted in figure 5(*d*) where a maximum is observed for case -1 (~ 1 % better than case 0). Therefore, the best solution found within the curvature range observed experimentally can be further improved with increased curvature. Nevertheless, within the experimentally observed curvature values we found that C-starts are the best escape mechanisms.
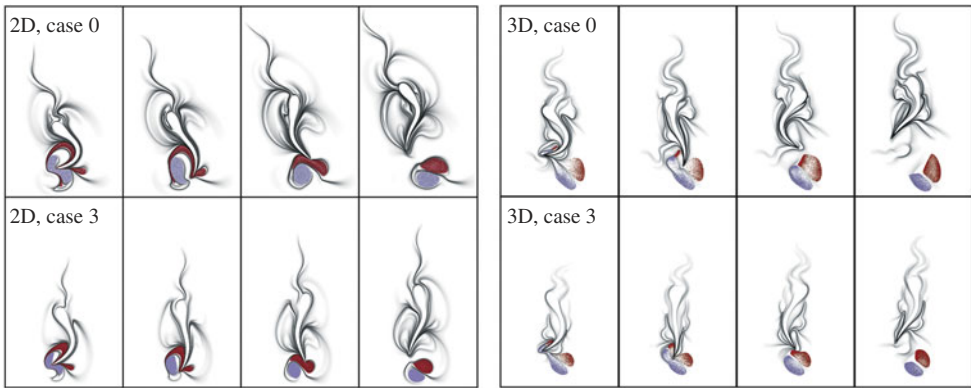
FIGURE 6. (Colour online) Particle tracking and F-FTLE time sequence ($0.5T_{prop} \leqslant t \leqslant 1.25T_{prop}$; $\Delta t = 0.25T_{prop}$). F-FTLE was computed given the integration time $T_{LE} = 1.59T_{prop}$.

The figure also shows the efficiency $\eta = (m/2)\,(\tau^{-1} \int_\tau \boldsymbol{U}\,\mathrm{d}t)^2/\int_\tau P\,\mathrm{d}t$ (where m and $\boldsymbol{U}$ are mass and velocity of the swimmer, P is the power imparted to the fluid and $\tau = T_{prep} + 2T_{prop}$, see appendix B – definition of efficiency) of the start procedure. We observe that the efficiency peaks between cases 2 and 3, and that the anguilliform start outperforms all C-starts. The plot also shows how C-starts are energetically inefficient, consistent with the observation that burst swimming modes are sustained for short time intervals by fish.

We performed particle tracking for case 0 (figure 6), advecting backwards in time passive particles initialized within vortical structure A, to qualitatively illustrate C-start dynamics. Particle locations are superimposed on a forward finite-time Lyapunov exponent (F-FTLE) field (Haller & Yuan 2000) to highlight regions of coherent flow behaviour. As can be noticed, particles are accelerated along the body, gaining momentum and circulation before being shed into a vortex pair. The fluid region trapped inside the area bounded by the C-shape of the larva, surrounded by the tracked particles, is accelerated as well and ejected opposite to the swimming direction, without much vorticity being generated. Figure 6 pictures the same analysis also for case 3, to illustrate how a smaller curvature corresponds to a smaller fluid region bounded by the C-shape. We conclude that increasing C-curvature results in stronger vortex pairs, which during their formation, due to transfer of momentum, contribute to the swimmer's acceleration, albeit at a decreased efficiency.

4.2. *Three-dimensional swimmer*

The evolution of the motion parameters for the three-dimensional case is shown in figure 2(b), and the best parameter set found is given in table 1. The most notable differences between the best parameters in three dimensions with respect to those in two dimensions are the reduced values of B_3 and B_4, indicating a smaller curvature of the posterior half of the fish during the preparatory stroke, and the increased values of K_3, K_4 and K_5, corresponding to larger curvatures during the propulsive stage. Compared to two dimensions, the complete motion in three dimensions differs in the continuous swimming phase, where the large curvature values of K_3–K_5 result in larger deformations of the body (figure 7). The forward velocity of the best three-dimensional larval fish is slightly smaller than in two dimensions, and reaches a maximum of 14 L s^{-1} during the propulsive stroke and 23 L s^{-1} during the ensuing swimming motion. Experimentally reported values for this fish at a similar Reynolds
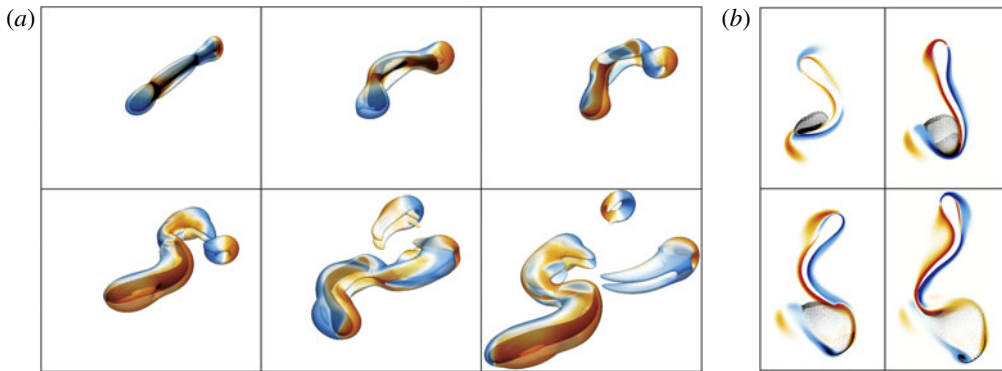
FIGURE 7. (Colour online) (*a*) Vorticity fields of the three-dimensional best solution found during the optimization (blue negative and red positive *z*-component of $\boldsymbol{\omega}$) time sequence at times t/T_{prop} 0.13, 0.43, 0.71, 1.04, 1.61 and 2.15 (left to right, top to bottom). Supplementary movie available at http://dx.doi.org/10.1017/jfm.2011.558. (*b*) Evolution of passive tracer particles seeded at $t/T_{prop} = 0.5$ and overlaid on the ω_z-field. Three sets of particles (dark–medium–light grey-scale) are initialized in different regions of the F-FTLE field. Sequence times as in figure 6.

number are $7\,L\,\mathrm{s}^{-1}$ for the propulsive stroke and swimming velocities between $14\,L\,\mathrm{s}^{-1}$ and $24\,L\,\mathrm{s}^{-1}$ (Muller *et al.* 2008). We observe that the simulated fish speeds are higher than those reported experimentally for the propulsive stroke while the speed of swimming motion is in good agreement with the experimental results.

The three-dimensional flow visualizations show that during the preparatory stroke, the larva tail generates a starting vortex ring travelling towards the swimmer's head. The formation of this vortex ring is not accompanied by significant acceleration of the body. During the first backflip of the tail (the propulsive stroke), the fish continuously generates vorticity along the complete profile of the tail. The resulting vortical structure is a vortex ring elongated along its top and bottom halves (figure 7), indicating a stronger vorticity generation at the top and bottom of the tail than at the middle as justified by the tail geometry. The vortical structures generated in subsequent swimming strokes are similar to this elongated vortex ring. The flow structures of the two-dimensional simulations and the mid-plane of the three-dimensional simulations are visually consistent with the experimental results reported in Muller *et al.* (2008) (figure 4). We remark that the elongated vortex rings that can be observed in the experimental results during the propulsive phase are also observed in the vorticity field of the three-dimensional simulations.

We have performed for the three-dimensional simulations a similar analysis as for the two-dimensional case by considering the vorticity field in the horizontal mid-plane, passing through the centre of mass of the fish (figure 8). We note similar trends for the circulation and area of the vortical structures A and B and fish speed. Also efficiency and distance travelled show a comparable behaviour between the two-dimensional and three-dimensional simulations, except for a larger difference in distance travelled between cases -1 and 0 ($\sim 4.5\,\%$). The particle tracking was performed for the three-dimensional simulation by placing the particles on the first vortex pair in the mid-plane of the swimmer (figure 6) and tracing the particles back in time. The particles stay on the mid-plane due to the vertical symmetry in the flow. However, contrary to the two-dimensional case, only few of the particles trace back to the
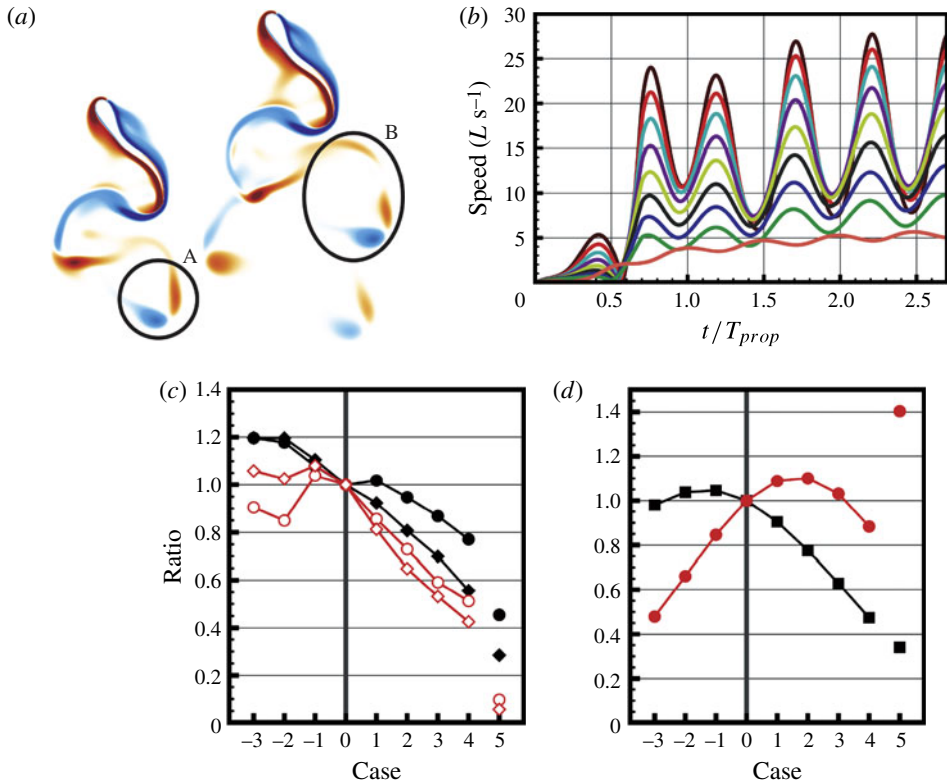
FIGURE 8. (Colour online) As figure 5 but for vortex ring characterization in the three-dimensional setup.

region bounded by the C-shape of the swimmer. A forward particle tracking was then performed to determine the path of the particles originating in the C-shape region (figure 7). The time frames show that the particles spread over a wide region behind the fish, bounded on two sides by a region of vorticity. This indicates that also in the three-dimensional case the fish accelerates a large region of fluid originating within the C-shape of the swimmer but the accelerated fluid spreads out over a much wider region than in the two-dimensional case.

5. Conclusions

We have performed a reverse engineering study of larval starting motions to identify the patterns which maximize the escape distance, coupling an evolution strategy with two- and three-dimensional flow simulations. The geometrical model, time scales and parameter search space were dictated by experimental observations of larval fish. The identified best motion kinematics are in good agreement with in *vivo* observations and exhibit C-start patterns, indicating that C-starts do indeed maximize the escape distance. The flow field is characterized by elongated vortex rings stretched by the zebrafish tail. The forward swimming velocities obtained in three-dimensional simulations are in good agreement with those measured in experiments while the vortical structures observed in the mid-plane are consistent with those reported in experiments (Muller *et al.* 2008). We find that the effectiveness of the C-start escape

relies on the ability of pronounced C-bent configurations to trap and accelerate large amounts of fluid. Furthermore C-starts are found to be energetically inefficient. A parametric investigation around our best solutions indicates that increasing curvatures beyond experimentally based bounds can lead to even larger escape distances. Future work will further investigate this latter observation and the multi-objective optimization of motion patterns using multi-resolution flow simulations.

Supplementary movies are available at http://dx.doi.org/10.1017/jfm.2011.558.

Appendix A. Larva's geometry

The geometrical aspect of the swimmer is characterized by the half width $w(s)$ of the body along its length, defined as:

$$w(s) = \begin{cases} w_h\sqrt{1 - \left(\dfrac{s_b - s}{s_b}\right)^2} & 0 \leqslant s < s_b \\[4mm] (-2(w_t - w_h) - w_t(s_t - s_b))\left(\dfrac{s - s_b}{s_t - s_b}\right)^3 + \\[4mm] (3(w_t - w_h) + w_t(s_t - s_b))\left(\dfrac{s - s_b}{s_t - s_b}\right)^2 + w_h & s_b \leqslant s < s_t \\[4mm] w_t - w_t\left(\dfrac{s - s_t}{L - s_t}\right)^2 & s_t \leqslant s \leqslant L \end{cases} \tag{A 1}$$

where L is the body length, $s_b = 0.0862L$, $s_t = 0.3448L$, $w_h = 0.0635L$ and $w_t = 0.0254L$. In the three-dimensional case, the geometry is described in terms of elliptical cross sections with width $w(s)$ and height $h(s)$, where $h(s)$ is given by

$$h(s) = \begin{cases} h_1\sqrt{1 - \dfrac{(s - s_1)^2}{s_1^2}} & 0 \leqslant s \leqslant s_1 \\[4mm] -2(h_2 - h_1)\left(\dfrac{s - s_1}{s_2 - s_1}\right)^3 + 3(h_2 - h_1)\left(\dfrac{s - s_1}{s_2 - s_1}\right)^2 + h_1 & s_1 < s \leqslant s_2 \\[4mm] -2(h_3 - h_2)\left(\dfrac{s - s_2}{s_3 - s_2}\right)^3 + 3(h_3 - h_2)\left(\dfrac{s - s_2}{s_3 - s_2}\right)^2 + h_2 & s_2 < s \leqslant s_3 \\[4mm] h_3\sqrt{1 - \left(\dfrac{s - s_3}{L - s_3}\right)^2} & s_3 < s \leqslant L. \end{cases} \tag{A 2}$$

Here we use the following parameter pairs: $(s_1, h_1) = (0.284L, 0.072L)$, $(s_2, h_2) = (0.844L, 0.041L)$ and $(s_3, h_3) = (0.957L, 0.071L)$.

Appendix B. Definition of efficiency

We define the efficiency as follows:

$$\eta = \frac{E_{useful}}{E_{flow}}, \tag{B 1}$$

where E_{useful} is the kinetic energy of the fish:

$$E_{useful} = \frac{1}{2}m\bar{U}^2, \tag{B 2}$$

with $\bar{U}$ the mean velocity of the fish during the simulation time ($T_{prep} + 2T_{prop}$) and m the fish mass.

The term E_{flow} represents the total energy delivered to the fluid,

$$\int_{\tau=0}^{T_{prep}+2T_{prop}} P_{flow}(t)\,\mathrm{d}\tau, \tag{B 3}$$

where P_{flow} is the total instantaneous power delivered to the fluid, which accounts for rate of change of kinetic energy and dissipation due to viscous stresses:

$$P_{flow} = \frac{d}{dt}\int_{\Omega_f} \rho\frac{u^2}{2}\,\mathrm{d}\Omega + \mu\int_{\Omega_f}\left(\boldsymbol{\nabla u} + (\boldsymbol{\nabla u})^T\right):\boldsymbol{\nabla u}\,\mathrm{d}\Omega, \tag{B 4}$$

with Ω_f denoting the spatial region occupied with fluid, and $u^2 = \boldsymbol{u}\cdot\boldsymbol{u}$.

Since we have a computational domain with free-space boundary conditions, the velocity field is not completely contained within the computational domain and the evaluation of the above integrals is not trivial. We will discuss the contribution of the velocity field outside our computational domain for each of the two terms in the right hand side of (B 4).

For the first term we first note that, for a divergence-free velocity field, the following kinematic identity holds Winckelmans & Leonard (1993):

$$\int_\Omega \boldsymbol{u}\cdot\boldsymbol{u}\,\mathrm{d}\Omega = \int_\Omega \boldsymbol{\Psi}\cdot\boldsymbol{\omega}\,\mathrm{d}\Omega. \tag{B 5}$$

Here Ψ is the streamfunction, defined as the solution of the Poisson equation

$$\nabla^2\boldsymbol{\Psi} = -\boldsymbol{\omega}, \tag{B 6}$$

hence $\boldsymbol{u} = \boldsymbol{\nabla}\times\boldsymbol{\Psi}$. The integral on the right-hand side can be computed in Fourier space from a compact vorticity field, and thus the kinetic energy in a domain with free-space boundary conditions can be computed as a function of the vorticity field only. To get the kinetic energy in the fluid domain only, we subsequently subtract the kinetic energy within the fish from this sum. Finally, the time derivative of the integral is computed as a first order finite difference between two timesteps.

In the current case, however, the velocity field inside the swimmer is not divergence free (due to the deformation velocity field of the swimmer – for more details refer to Gazzola *et al.* (2011*a*)). The integral in (B 5) therefore is an incomplete measure of the total kinetic energy since it neglects the contribution of the potential to the velocity field. After initial tests comparing the influence of the potential, however, we observed that this contribution to both the total kinetic energy as well as its time-derivative was several orders of magnitude smaller than the contribution from the stream function. To save in computational costs we therefore chose to neglect the contribution from the potential and base the efficiency on the kinetic energy due to the vorticity-induced velocity only.

The second integral in (B 4) represents the viscous dissipation term. By systematically increasing the domain size, we found that the contribution this increase

is negligible and we therefore compute this integral only inside the computational domain.

REFERENCES

BUCHE, D., STOLL, P., DORNBERGER, R. & KOUMOUTSAKOS, P. 2002 Multiobjective evolutionary algorithm for the optimization of noisy combustion processes. *IEEE Trans. Syst. Man Cybern.* C **32** (4), 460–473.

BUDICK, S. A. & O'MALLEY, D. M. 2000 Locomotor repertoire of the larval zebrafish: swimming, turning and prey capture. *J. Expl Biol.* **203** (17), 2565–2579.

CONTE, J., MODARRES-SADEGHI, Y., WATTS, M. N., HOVER, F. S. & TRIANTAFYLLOU, M. S. 2010 A fast-starting mechanical fish that accelerates at 40 m s$^{(-2)}$. *Bioinspir. Biomim.* **5** (3).

COQUERELLE, M. & COTTET, G. H. 2008 A vortex level set method for the two-way coupling of an incompressible fluid with colliding rigid bodies. *J. Comput. Phys.* **227** (21), 9121–9137.

DOMENICI, P. & BLAKE, R. W. 1997 The kinematics and performance of fish fast-start swimming. *J. Expl Biol.* **200** (8), 1165–1178.

EPPS, B. P. & TECHET, A. H. 2007 Impulse generated during unsteady maneuvering of swimming fish. *Exp. Fluids* **43** (5), 691–700.

FONTAINE, E., LENTINK, D., KRANENBARG, S., MULLER, U. K., VAN LEEUWEN, J. L., BARR, A. H. & BURDICK, J. W. 2008 Automated visual tracking for studying the ontogeny of zebrafish swimming. *J. Expl Biol.* **211** (8), 1305–1316.

GAZZOLA, M., CHATELAIN, P., VAN REES, W. M. & KOUMOUTSAKOS, P. 2011*a* Simulations of single and multiple swimmers with non-divergence free deforming geometries. *J. Comput. Phys.* **230** (19), 7093–7114.

GAZZOLA, M., VASILYEV, O. V. & KOUMOUTSAKOS, P. 2011*b* Shape optimization for drag reduction in linked bodies using evolution strategies. *Comput. Struct.* **89** (11–12), 1224–1231.

HALLER, G. & YUAN, G. 2000 Lagrangian coherent structures and mixing in two-dimensional turbulence. *Physica* D **147** (3–4), 352–370.

HANSEN, N., MULLER, S. D. & KOUMOUTSAKOS, P. 2003 Reducing the time complexity of the derandomized evolution strategy with covariance matrix adaptation (cma-es). *Evolutionary Computation* **11** (1), 1–18.

HOWARD, C. H. 1974 Optimal strategies for predator avoidance: the relative importance of speed and manoeuvrability. *J. Theor. Biol.* **47** (2), 333–350.

HU, W. R., YU, Y. L., TONG, B. G. & LIU, H. 2004 A numerical and analytical study on a tail-flapping model for fish fast c-start. *Acta Mechanica Sin.* **20** (1), 16–23.

KATUMATA, Y., MULLER, U. K. & LIU, H. 2009 Computation of self-propelled swimming in larva fishes. *J. Biomech. Sci. Engng* **4** (1), 54–66.

KERN, S. & KOUMOUTSAKOS, P. 2006 Simulations of optimized anguilliform swimming. *J. Expl Biol.* **209** (24), 4841–4857.

KOUMOUTSAKOS, P. 1997 Inviscid axisymmetrization of an elliptical vortex. *J. Comput. Phys.* **138** (2), 821–857.

KOUMOUTSAKOS, P. & LEONARD, A. 1995 High-resolution simulations of the flow around an impulsively started cylinder using vortex methods. *J. Fluid Mech.* **296**, 1–38.

MULLER, U. K., VAN DEN BOOGAART, J. G. M. & VAN LEEUWEN, J. L. 2008 Flow patterns of larval fish: undulatory swimming in the intermediate flow regime. *J. Expl Biol.* **211** (2), 196–205.

MULLER, U. K. & VAN LEEUWEN, J. L. 2004 Swimming of larval zebrafish: ontogeny of body waves and implications for locomotory development. *J. Expl Biol.* **207** (5), 853–868.

PARICHY, D. M., ELIZONDO, M. R., MILLS, M. G., GORDON, T. N. & ENGESZER, R. E. 2009 Normal table of postembryonic zebrafish development: staging by externally visible anatomy of the living fish. *Dev. Dyn.* **238** (12), 2975–3015.

TYTELL, E. D. & LAUDER, G. V. 2002 The c-start escape response of polypterus senegalus: bilateral muscle activity and variation during stage 1 and 2. *J. Expl Biol.* **205** (17), 2591–2603.

WALKER, J. A., GHALAMBOR, C. K., GRISET, O. L., MCKENNEY, D. & REZNICK, D. N. 2005
   Do faster starts increase the probability of evading predators? *Funct. Ecol.* **19** (5), 808–815.

WEIHS, D. 1973 The mechanism of rapid starting of slender fish. *Biorheology* **10**, 343–350.

WEIHS, D. & WEBB, P. W. 1984 Optimal avoidance and evasion tactics in predator–prey
   interactions. *J. Theor. Biol.* **106** (2), 189–206.

WINCKELMANS, G. S. & LEONARD, A. 1993 Contributions to vortex particle methods for the
   computation of three-dimensional incompressible unsteady flows. *J. Comput. Phys.* **109**,
   247–273.